International Journal of
Plasma Environmental Science and Technology

*Regular Paper*

DOI: 10.34343/ijpest.2021.15.e02007

# *In situ* Raman spectroscopy of plasma–catalyst interface for conversion of $CO_2$ and $CH_4$ to valuable compounds

**Atsushi Saito[1,2], Zunrong Sheng[1], Tomohiro Nozaki[1,*]**

[1] Department of Mechanical Engineering, Tokyo Institute of Technology, Japan
[2] AGC Inc., Japan

* Corresponding author: nozaki.t.ab@m.titech.ac.jp (Tomohiro Nozaki)

Received: 18 April 2021
Revised: 7 June 2021
Accepted: 13 June 2021
Published online: 15 June 2021

## Abstract

This study demonstrates the reduction of carbon dioxide ($CO_2$) via a plasma–catalyst hybrid process in the presence of methane ($CH_4$) and hydrogen ($H_2$). Dielectric barrier discharge (DBD) plasma-activated $Ar/CO_2/CH_4/H_2$ was applied to copper nanoparticles supported on zinc oxide (ZnO). The surface species and their reaction pathways were investigated via *in situ* Raman spectroscopy under DBD irradiation. The Raman shift peaks were identified from literature review and density functional theory (DFT) calculations. Acetate ($CH_3COO$) was produced as the reaction product via a DBD -induced surface reaction. In addition, acetaldehyde ($CH_3CHO$) was produced by irradiation with DBD -activated $H_2O$. The conversion of $CO_2$ and $CH_4$ to valuable compounds was evaluated via *in situ* observations, and the reaction pathway was examined.

**Keywords:** $CO_2$ conversion, carbon recycling, *in situ* Raman spectroscopy, plasma catalysis.

## 1. Introduction

Technological developments based on carbon recycling are being actively promoted to reduce carbon dioxide ($CO_2$) emissions [1, 2]. A catalytic reduction process has been developed to convert $CO_2$ into valuable resources. Methane ($CH_4$) is abundant, and dry methane reforming offers significant benefits in the upgradation of biogas to syngas [3, 4] and reduction of greenhouse gas emissions. However, this process requires high-temperature thermal energy, which inevitably involves the combustion of either initial feed or off gas. Thus, this results in $CO_2$ generation, which is not suitable from the carbon recycling perspective [5].

Researchers have been investigating processes that use renewable electricity to reduce $CO_2$ emissions. Most of these processes are based on electrochemical reactions [6]; however, photochemical and photoelectrochemical processes [7] that directly use solar energy have recently been reported. In addition, the use of nonthermal plasma generated by renewable electricity has also been considered. A promising technique is the application of a nonthermal plasma–catalyst hybrid reaction. Plasma-excited $CO_2$ or hydrogen reacts with heterogeneous catalysts during plasma catalysis [8, 9], enabling the conversion of $CO_2$ into valuable chemicals at low temperatures [10].

Processes that are currently under development as plasma catalysis include $CH_4$ reforming with $CO_2$ [11] and direct $CO_2$ conversion to the building block of C1 chemistry [12,13]. In plasma catalysis, the gas is directly activated and used for the reaction. Therefore, hydrogen produced by the electrolysis of water is not used in this process. In addition, the use of plasma has been investigated in methanation [14], methanol synthesis [15], and water–gas shift reaction [16].

This study examines the plasma catalysis reaction and analyzes the surface reaction dynamics for the synthesis of valuable compounds, a promising approach for $CO_2$ conversion in the presence of $CH_4$. Plasma is generated via dielectric barrier discharge (DBD) [17], which is often used as a high-pressure nonthermal plasma source [18]. A hybrid plasma and catalyst process can be achieved at low temperatures; however, the

reaction mechanism is complex and yet to be fully understood. Plasma produces various types of active species through an intricate production pathway. In addition, active species react in the gas phase and on solid surfaces. A nonthermal plasma-induced surface reaction was analyzed via *in situ* infrared spectroscopy under DBD irradiation to identify the surface adsorbates. To elucidate the reaction mechanism, evaluation using diffuse reflectance infrared Fourier transform spectroscopy (DRIFTS) was conducted [19, 20, 21]. However, even in the *in situ* evaluation, it is difficult to understand the details of the highly reactive surface reaction unless the evaluation is performed while irradiating with plasma.

In this study, an *in situ* Raman spectroscopy (RS) system for plasma catalysis was developed, and copper (Cu) nanoparticles supported on zinc oxide (ZnO) were irradiated with DBD-activated $CO_2$ and $CH_4$ to simultaneously measure the surface reaction. This is a unique system that not only can evaluate the surface on which plasma is applied without exposing it to the atmosphere, but can also measure the surface under plasma irradiation at the same time. From technological viewpoint, Raman spectroscopy uses the excitation laser in the visible light region, and thus plasma reactor and optical systems can be constructed by standard materials such as quartz window. Scattered light can be collected and introduced into the spectrometer, the device configuration is simple as an *in situ* evaluation system; thus, it is easy to install the plasma source and heating component. More importantly, infrared (IR) and Raman spectroscopy provide complementary spectroscopic information; thus, we have developed *in situ* Raman spectroscopy that can be combined with IR analysis in the future. Surface species were analyzed by vibration analysis using density functional theory (DFT) calculations to investigate unstable species and the reaction pathway [22].

## 2. Experimental

### 2.1 *In situ* RS system under plasma irradiation

ZnO powder (48044-13, Kanto Chemical Co., Inc.) was compressed at 1.5 MPa to obtain 1 mm thick tablets of ⌀10 mm. The Cu nanoparticles were sputtered directly onto the tablet. The Cu was deposited at a process pressure of 0.6 Pa at room temperature. The size of the Cu nanoparticles was controlled by the sputtering time, and a film with a thickness of 3 nm was formed. Fig. 1 (a) presents the schematic of the reactor, whereas Fig. 1(b) presents a photograph of the plasma emission and Raman excitation laser. The emissions from the plasma and Raman excitation laser were observed simultaneously. The reaction cell was composed of glass, and a quartz window was placed in front of the glass reactor. The DBD was generated inside a quartz tube to generate a plasma jet, where the ground electrode was wrapped around the quartz tube. The input peak-to-peak voltage for the DBD was 8–15 kV with an alternating-current frequency of 15 kHz.

A mixture of Ar, $CO_2$, $CH_4$, and $H_2$ was introduced into the reactor via mass flow controllers. In addition, $H_2O$ was introduced by bubbling Ar. The water tank was heated using a heater, and the temperature of the $H_2O$ in the tank was set to 348 K. After the catalyst tablet was set, Ar was introduced and allowed to flow for 10 min. Background Raman spectrum was obtained at this time.

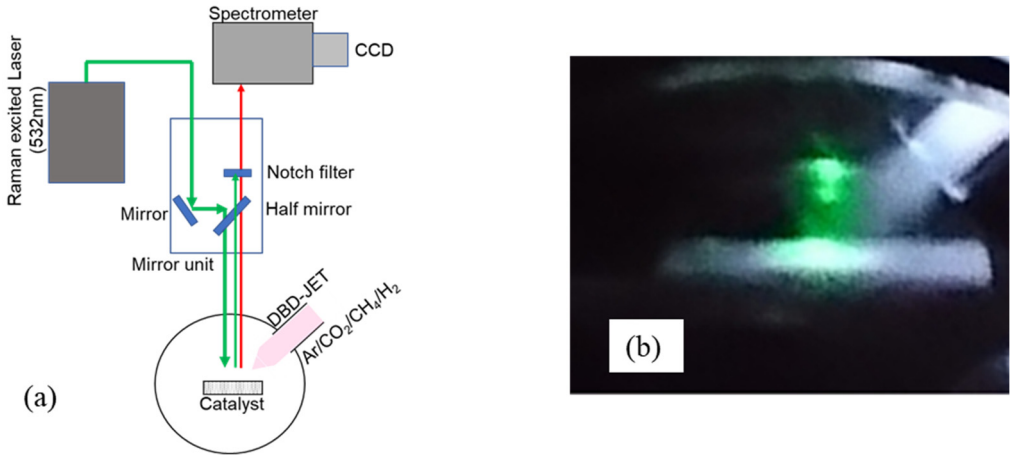


**Fig. 1.** (a) Schematic of the *in situ* Raman system and (b) photograph of simultaneous dielectric barrier discharge (DBD) irradiation and laser emission.

### 2.2 Vibration analysis of catalytic surface species via DFT

Vibration analysis was performed via DFT using a Cu and ZnO surface cluster model. Gas adsorption primarily occurs on the surface of cubic Cu (111) and hexagonal ZnO (100) [23]. Thus, various surface species were produced on the cubic Cu (111) and hexagonal ZnO (100), and the optimized structure was determined. The (100) surface of hexagonal ZnO [24] was demonstrated in Section 3.1; thus, a two-layer model of the (100) surface of hexagonal ZnO was constructed for DFT calculations. The initial geometrical parameters of the (100) ZnO surface model were obtained from the X-ray structure illustrated in Fig. 3 (a). The chemical species were placed on the first layer of the ZnO surface model. The second layer was fixed, and the chemical species and first layer were allowed to completely relax. Although some imaginary frequencies appeared for the chemical species in $CH_3CHO$, they primarily originated from the second layer rather than the first, indicating that the vibration analysis was less affected by the imaginary frequencies. All calculations were performed at the B3LYP[25]/ 6-31G**[26] level using Gaussian 16 [27]. Vibration analysis was performed after structural optimization [28, 29, 30].

## 3. Results and discussion

### 3.1 Observation of Cu nanoparticles on ZnO catalyst

A scanning electron microscopy (SEM, SU8030, Hitachi High-Tech) image of Cu/ZnO is presented in Fig. 2, and the X-ray diffraction (XRD) spectra (Smart Lab, Rigaku) are presented in Fig. 3 (a) and (b). It can be observed that the size of the Cu nanoparticles was approximately 10 nm. In regards to the crystal structure, it can also be observed that Cu has a cubic crystal structure and ZnO has a hexagonal crystal structure [23].

### 3.2 Surface analysis with X-ray photoelectron spectroscopy

X-ray photoelectron spectroscopy (XPS; Quantera SXM, ULVAC PHI) analysis was performed to determine the change in the sample surface after DBD irradiation. The plasma irradiation time was 10 min. The results are presented in Fig. 4. XPS analysis was performed on three samples: (a) as-prepared catalyst (reference), (b) $Ar/H_2/CH_4/CO_2$ gas only (without DBD), and (c) DBD-activated $Ar/H_2/CH_4/CO_2$. Furthermore, Fig. 5 presents the quantitative analysis of the surface functional groups calculated from the peak fitting depicted in Fig. 4. The effect of the surface treatment was changed by the irradiation of DBD. In particular, the C=C–O, C=O, and C–O–C bond-peak intensities increased [31, 32]. These were the effects of plasma-activated $CO_2$, $CH_4$, and $H_2$ reactants.

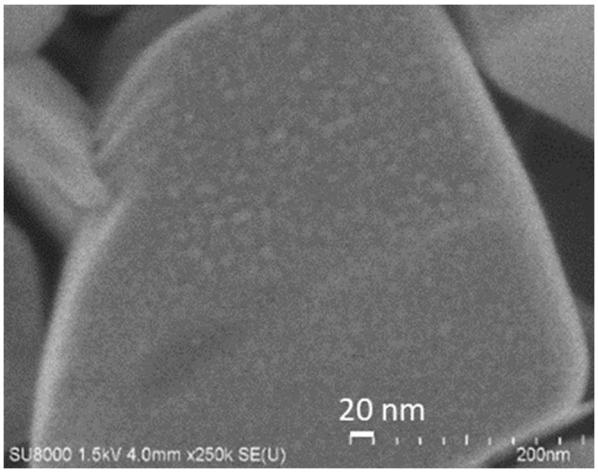


**Fig. 2.** Scanning electron microscopy (SEM) image of Cu nanoparticles on ZnO.

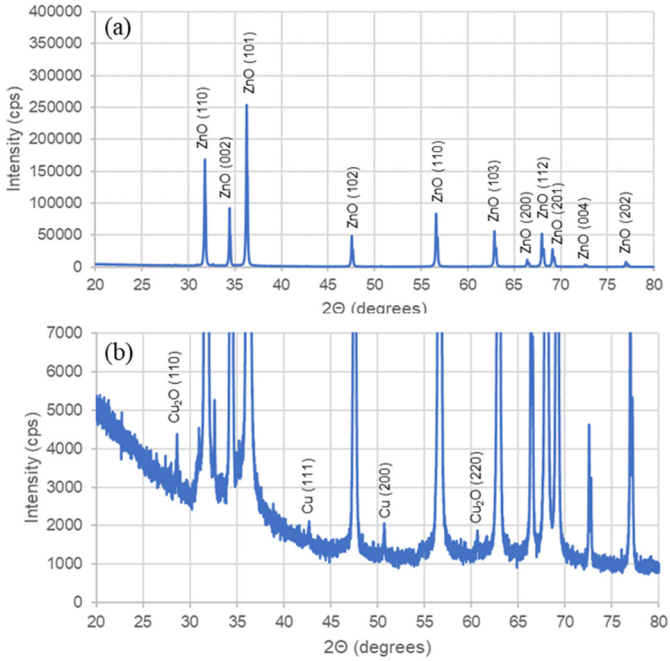


**Fig. 3.** X-ray diffraction (XRD) spectrum of (a) Cu nanoparticles on ZnO. (b) Enlarged image of the spectrum shown in (a).

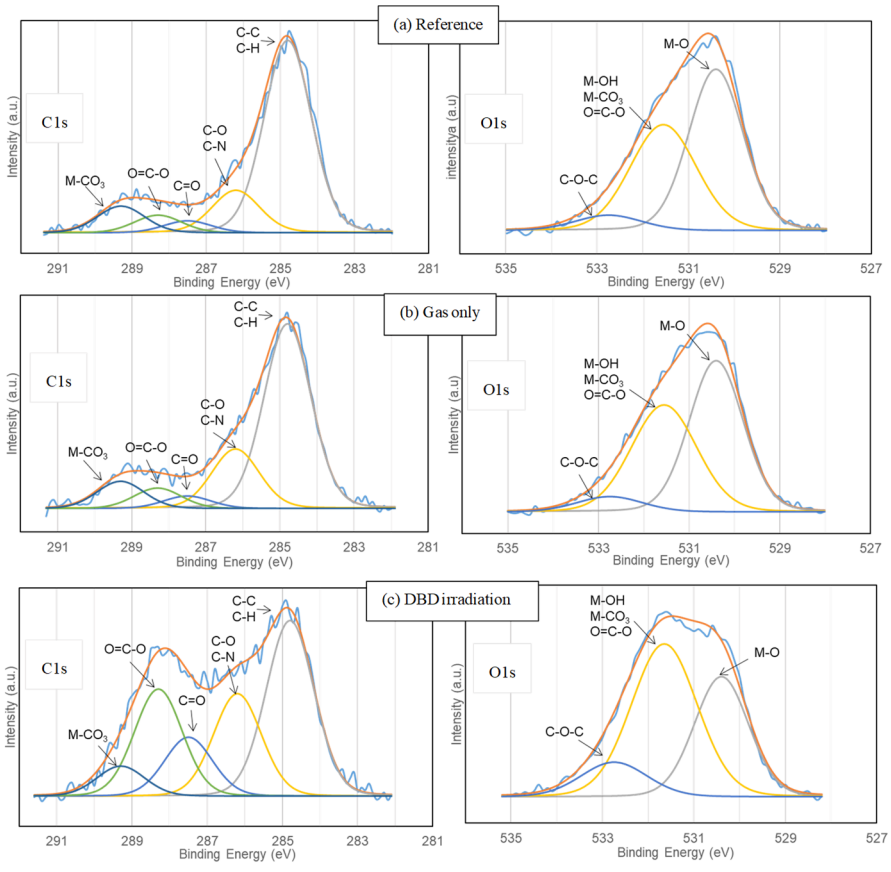


*Reference is as-prepared Cu/ZnO catalyst.

*Reference is as-prepared Cu/ZnO catalyst.

**Fig. 4.** X-ray photoelectron spectroscopy (XPS) analysis results of Cu/ZnO. The graphs on the left display the C1s spectra, whereas those on the right display the O1s spectra. (a) Reference indicates as-prepared catalyst sample, (b) Gas only indicates no DBD activation, and (c) DBD irradiation indicates activated gas irradiation for Cu/ZnO. The gases introduced were $Ar/CO_2/CH_4/H_2$ = 100/180/40/40 $cm^3$ $min^{-1}$, the input voltage was 9 $kV_{pp}$, and the alternating-current frequency was 15 kHz.

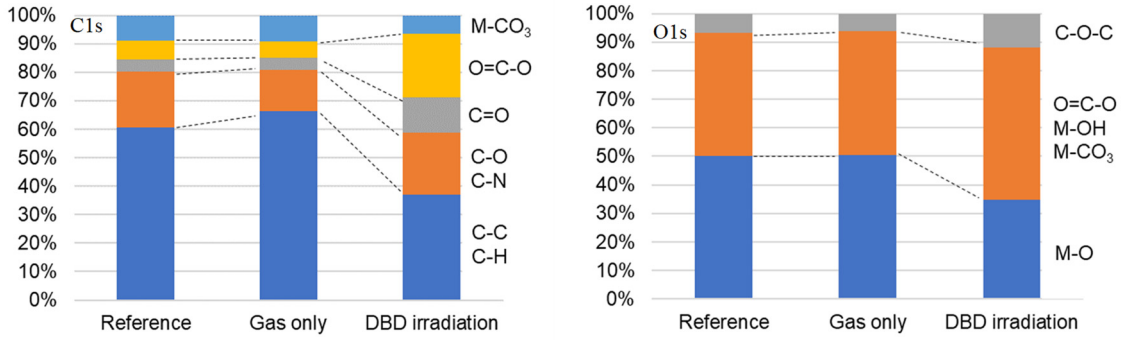


*Reference is as-prepared Cu/ZnO catalyst.
*M in the graph indicates metal (Zn or Cu).

**Fig. 5.** Quantitative evaluation of surface functional groups via XPS. Reference indicates as-prepared catalyst sample, Gas only indicates no DBD activation, and DBD irradiation indicates activated gas irradiation for Cu/ZnO. The gases introduced were $Ar/CO_2/CH_4/H_2$ = 100/180/40/40 $cm^3$ $min^{-1}$, the input voltage was 9 $kV_{pp}$, and the alternating-current frequency was 15 kHz.

### 3.3 *In situ* Raman spectroscopy of DBD-irradiated Cu/ZnO

Fig. 6 presents the results of the $CH_4$-dependent *in situ* RS of DBD-activated $Ar/CO_2/CH_4$ irradiated on ZnO. When the surface temperature of the catalyst during plasma irradiation was confirmed using a thermocamera, it was observed to be lower than 373 K. By increasing the amount of $CH_4$, a new peak emerged at 3030 $cm^{-1}$, which is assigned as a CH vibration. When the $CH_4$ flow rate was further increased, a new peak appeared near 1550 $cm^{-1}$. This could be attributed to the D-band peak due to amorphous carbon deposition; however, this peak disappeared when the gas was switched to Ar. Ideally, this peak should not disappear when the gas is switched to Ar because amorphous carbon is stable at ambient conditions. Therefore, it is considered that this peak does not correspond to the carbon thin film. According to the literature, this peak can be related to adsorbed hydrocarbons [33].

Fig. 7 presents the results of *in situ* RS of activated $Ar/CO_2/CH_4/H_2$ irradiated on Cu/ZnO depending on the $H_2$ flow rate. H can also be obtained by decomposing $CH_4$, but $H_2$ was introduced as an additive gas to verify the effect of hydrogenation. The addition of 10 $cm^3$ $min^{-1}$ of $H_2$ drastically increased the peak at approximately 1550 $cm^{-1}$. This indicates that activated $H_2$ reacted with the adsorbed $CO_2$, and its reaction intermediate reacted with the surface $CH_4$ species. However, when excessive $H_2$ was introduced, the peak intensity was reduced. This indicates that there are multiple reaction intermediates in the reaction between $H_2$ and $CO_2$. Further, $CH_4$ is adsorbed on Cu as $CH_3$ [34], and DBD promoted $CH_4$ chemisorption. $CH_4$ is vibrationally excited in the plasma [35], followed by adsorbed on Cu at low temperature. The peak at 3030 $cm^{-1}$ depicted in Fig. 6 (b)–(d) and Fig. 7 (a) is considered to be $CH_3$ and represents CH stretching vibration [36]. A peak appeared at 1550 $cm^{-1}$ when $CH_4$ was introduced (Fig. 6). Vibrationally excited $CO_2$ is known to react with oxygen anions on the oxide and form carbonate [35, 37]. Chemical species corresponding to 1550 $cm^{-1}$ were formed by the reaction of adsorbed $CH_3$ on Cu or carbonate. In addition, they were formed via direct reactions with $CH_3$ and vibrationally excited $CO_2$. A 1550 $cm^{-1}$ peak was generated by the $H_2$ admixture, as illustrated in Fig. 7 (b) and (c). The adsorption of hydrogen on Cu and ZnO was promoted by plasma-induced activation. On the surface of ZnO, Zn with dangling bonds and H bonded to O were formed to generate surface defects. Activated $CO_2$ was adsorbed on the oxygen anion ($O^{2-}$) of ZnO to form carbonate ($CO_3^{2-}$). Thereafter, it reacted with the adsorbed $CH_3$ on Cu. This reaction can be considered as the Langmuir–Hinshelwood mechanism. It is conceivable that activated $CO_2$ reacts directly with $CH_3$ to form an intermediate product and is considered to follow the Eley–Rideal mechanism.

It is possible that activated $CH_4$ reacted directly with carbonate on ZnO to form an intermediate product; however, this peak was not observed on the surface without Cu. Therefore, a carbonate or $CH_4$ reaction via the Eley–Rideal mechanism is unlikely. Activated $CO_2$ is vibrationally excited by the collision of electrons in the plasma. Subsequently, when hydrogen was introduced, $CO_2$ reacted with the activated hydrogen in the gas phase to generate CO. Meanwhile, the adsorbed species were reduced by excess activated $H_2$. Therefore, the amount of vibrationally excited $CO_2$ was reduced, and the formation of intermediate products was reduced.

Fig. 8 presents the results of peak separation at 1200–1700 $cm^{-1}$ in Fig. 7 (b). The results indicate that there are three components: 1341, 1441, and 1555 $cm^{-1}$. The species corresponding to these peaks have been attributed to acetate ($CH_3COO$) in the literature [38, 39]. Notably, the difference is minimal and in good agreement with the results from the DFT calculations. Table 1 presents a comparison between the experimental results, cited literature, and DFT calculations.

In addition, although peak separation was attempted at around 3000 $cm^{-1}$, it could not be performed because the intensity and signal-to-noise ratio were extremely low and thus difficult to control.

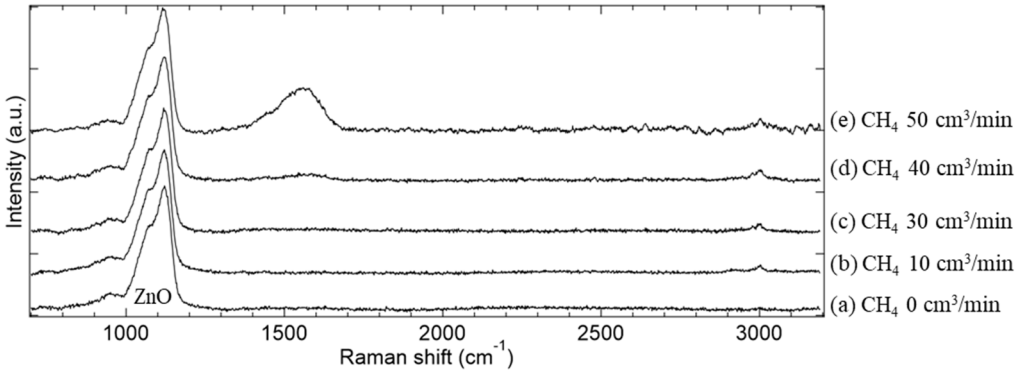


**Fig. 6.** Effect of $CH_4$ flow rate on the formation of adsorbed species with DBD-activated Ar/ $CO_2$ /$CH_4$ irradiation on Cu/ZnO tablets. The Ar and $CO_2$ flow rates are 100 and 80 $cm^3$ $min^{-1}$, respectively. The applied voltage is 9 $kV_{pp}$, and the alternating-current frequency is 15 kHz. The $CH_4$ flow rate of (a), (b), (c), (d), and (e) are 0, 10, 30, 40, and 50 $cm^3$ $min^{-1}$, respectively.

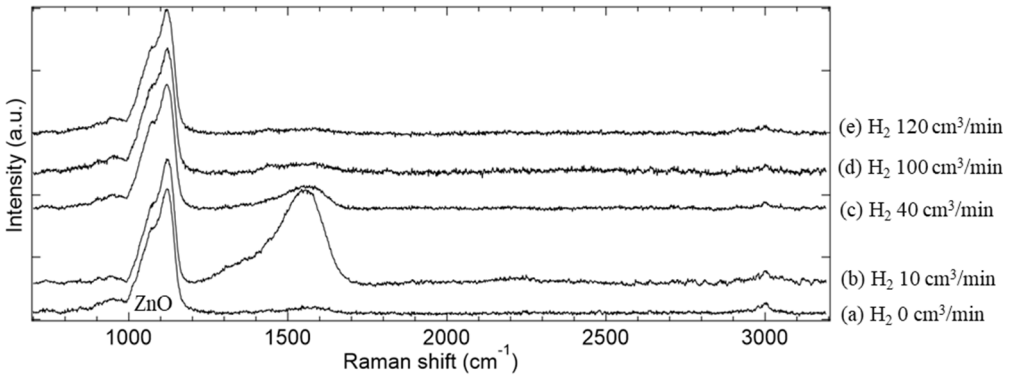


**Fig. 7.** Effect of $H_2$ flow rate upon *in situ* Raman spectroscopy results of dielectric barrier discharge (DBD)-activated Ar/ $CO_2$ /$CH_4$ /$H_2$ irradiation on Cu/ZnO tablets. The Ar, $CO_2$, and $CH_4$ flow rates are 100, 80, and 40 $cm^3$ $min^{-1}$, respectively. The applied voltage for DBD is 9 $kV_{pp}$, and the alternating-current frequency is 15 kHz. The $H_2$ flow rates of (a), (b), (c), (d), and (e) are 0, 10, 40, 100, and 120 $cm^3$ $min^{-1}$, respectively.

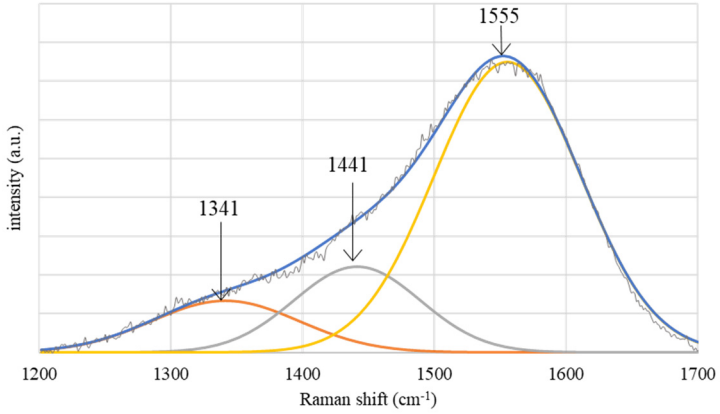


**Fig. 8.** Peak separation results in the 1200–1700 $cm^{-1}$ region of Fig. 7 (b).

**Table 1.** Comparison of frequency ($cm^{-1}$) of *in situ* Raman spectroscopy experimental values, density functional theory (DFT) calculations, literature values for various vibrational modes, and the structural optimization in DFT calculations of $CH_3COO$ on ZnO.

| *In situ* RS | DFT ($cm^{-1}$) | Literature ($cm^{-1}$) | Vibrational mode | |
|---|---|---|---|---|
| 1341 | 1334 | | $CH_3$ bending-1 (out-of-plane, sym.) | |
| | 1400 | 1414 | $CH_3$ bending-2 (out-of-plane, sym.) and C–C stretching | |
| 1441 | 1418 | 1430 | $CH_3$ bending-3 (out-plane, asym.) | |
| | 1440 | 1443 | $CH_3$ bending-4 (out-plane, asym.) | |
| 1555 | 1556 | 1578 | O–C–O stretching (asym.) | |
| | 2943 | 2936 | $CH_3$ stretching-1 (sym.) | |
| 3030 | 3015 | 2989 | $CH_3$ stretching-2 (asym.) | |
| | 3052 | | $CH_2$ stretching (asym.) | |

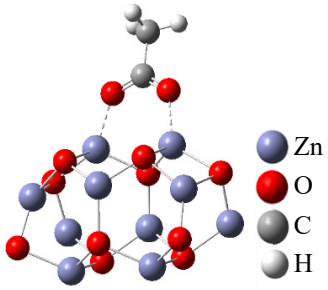


### 3.4 Effect of DBD-activated $H_2O$

The effect of DBD-activated $H_2O$, as a by-product of $CO_2/CH_4$ reaction, was examined for further hydrogenation of the surface-adsorbed $CH_3COO$, as evaluated in Section 3.3. In hydrogenation with DBD-activated $H_2$, the peak decreases owing to the high reactivity of $H_2$, as shown in Section 3.3. Therefore, the details of the reaction were investigated using $H_2O$, which has a low reactivity for hydrogenation. $H_2O$ was introduced by bubbling water and heated to 348 K with Ar. The effects of DBD-activated $H_2O$ are illustrated in Fig. 9. As depicted in Fig. 9 (b), the introduction of $H_2O$ without DBD did not change the spectrum. Moreover, it can be observed from Fig. 9 (c) that the peak around 1580 $cm^{-1}$ is narrower and has been shifted to a higher wave number. Fig. 10 shows the results of peak separation at 1200–1700 $cm^{-1}$, corresponding to Fig. 9 (c). It was observed that this contained a separate peak at 1601 $cm^{-1}$, which was different from that at 1555 $cm^{-1}$ and attributed to $CH_3COO$. In addition, new peaks emerged at 1305, 1425, 1720, 1824, 1913, 2950 and 3068 $cm^{-1}$. The $H_2O$ activated by the DBD is considered to be vibrationally excited $H_2O$. From the DFT calculations, the resulting peaks at 1305, 1425, 1601, 2950, and 3068 $cm^{-1}$ that appeared could be attributed to acetaldehyde ($CH_3CHO$). Table 2 presents a comparison between the experimental results and DFT calculations [41]. The peaks at 1720, 1824, and 1913 $cm^{-1}$ could not be identified using DFT. The peak of H adsorbed on the surface appeared in this region [42] is thought to result from the adhesion of H generated by the decomposition of DBD-activated $H_2O$ [40].

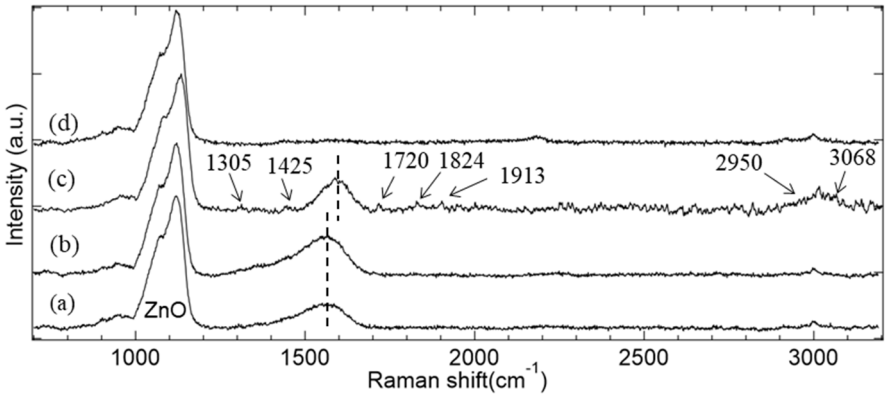


**Fig. 9.** Effect of $H_2O$ irradiation on the surface of Cu/ZnO tablets after Ar/$CO_2$/$CH_4$/$H_2$ plasma treatment measured via *in situ* Raman spectroscopy. (a) Spectrum irradiated with dielectric barrier discharge (DBD)-activated Ar/$CO_2$/$CH_4$/$H_2$. (b) Result of irradiating $H_2O$ after treatment of (a). (c) Result of irradiating DBD-activated $H_2O$ after treatment of (b). (d) Result of maintaining an Ar atmosphere after processing (c). $H_2O$ is introduced by bubbling Ar, maintaining the water tank at 348 K. The Ar flow rate for bubbling is 100 $cm^3$ $min^{-1}$. The Ar, $CO_2$, $CH_4$, and $H_2$ flow rates are 100, 80, 40 and 40 $cm^3$ $min^{-1}$, respectively. The applied voltage for DBD is 9 $kV_{pp}$, and the alternating-current frequency is 15 kHz.

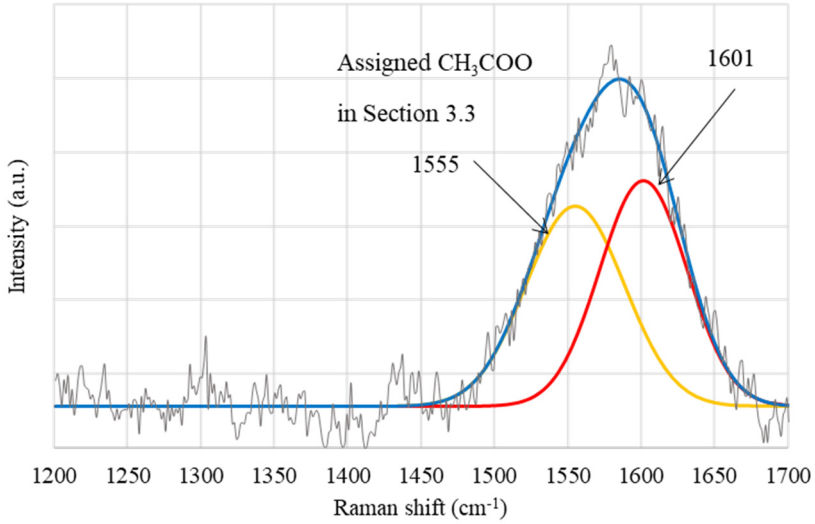


**Fig. 10.** Peak separation results in the 1200–1700 $cm^{-1}$ region of Fig. 9 (c).

### 3.5 Reaction mechanism governing the plasma effect on the ZnO surface

The reaction between the DBD-activated Ar/$CO_2$/$CH_4$/$H_2$ and Cu nanoparticles on ZnO is as follows. Active species adsorbed on the surface are indicated by "*". Vibrationally excited state are indicated by "$^v$". Reactions (R1–R14) are described below. Hydrogen atoms were generated by the collision of electrons (R1) and the hydrogen atoms bound to ZnO and Cu (R2). $H_2O$ was vibrationally excited by electrons to produce $H_2O^v$ (R3), and H* and OH* were generated on the surface (R4) [40]. In addition, the electrons collided with $CH_4$ to generate $CH_4^v$ (R5) [11,35]. $CH_4^v$ produced $CH_3$* and H* on Cu (R6), and $CO_2$ produced CO (R7) [43] and $CO_2^v$ (R8) via electron collisions. $CO_2$ reacted with H to form CO and $H_2O$ (R9) and combined with the oxygen anion sites ($O^{2-}$*) to form $CO_3^{2-}$*on ZnO surface (R10) [44].

$CH_3$* and $CO_3^{2-}$* on the surface of ZnO formed $CH_3COO$* and $O^{2-}$* (R11). Meanwhile, vibrationally excited $CH_4$ and $CO_3^{2-}$* are unlikely to react to produce $CH_3COO$*. This is because $CH_3COO$ was not generated on the ZnO surface without Cu. This indicates that $CH_3$ adsorbed on Cu (R6) is required for the generation of $CH_3COO$*. Additionally, $CO_2^v$ and $CH_3$* on Cu formed $CH_3COO$* (R12). It has been reported in the literature that H and $CO_3^{2-}$ on the surface form HCOO* [35]. In addition, $CO_2^v$ reacts with H* to form HCOO* [45, 46]. $CH_4^v$ and $CO_2^v$ directly interact with surface species in these reactions, considered to follow the Eley–Rideal mechanism.

**Table 2.** Comparison of frequency ($cm^{-1}$) of *in situ* Raman spectroscopy experimental values, density functional theory (DFT) calculations for various vibrational modes, and the structural optimization in DFT calculations of $CH_3CHO$ on ZnO.

| *In situ* RS | DFT ($cm^{-1}$) | Vibrational mode | |
|---|---|---|---|
| 1305 | 1337 | $CH_3$ bending-1 (out-of-plane, sym.) | 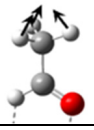 |
| | 1395 | H–C–C bending (in-plane) |  |
| 1425 | 1409 | $CH_3$ bending-2 (out-plane, asym.) | 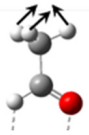 |
| | 1418 | $CH_3$ bending-3 (out-plane, asym.) | 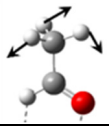 |
| 1601 | 1669 | CO stretching | 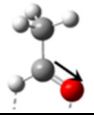 |
| | 2898 | CH stretching | 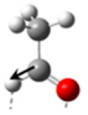 |
| 2950 | 2922 | $CH_3$ stretching-1 (sym.) |  |
| | 2978 | $CH_2$ stretching (asym.) | 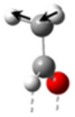 |
| 3068 | 3046 | $CH_3$ stretching-2 (asym.) | 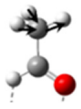 |

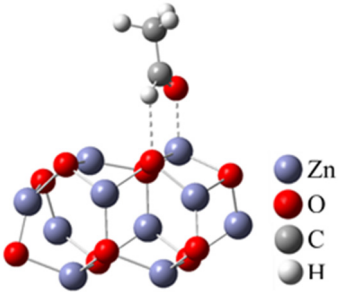


Because $CH_3CHO$* is generated when $H_2O^v$ reacts with $CH_3COO$*, as depicted in Section 3.4, Fig.9 (c), H or H* generated from DBD-activated $H_2$ did not contribute toward the reaction. Therefore, $CH_3CHO$ was generated by the reaction of H* generated from $H_2O^v$ with $CH_3COO$* (R13), and this reaction was considered to progress by the Langmuir–Hinshelwood mechanism.

$$H_2 + e^- \rightarrow 2H + e^- \quad \text{(R1)}$$

$$H \rightarrow H^* \quad \text{(R2)}$$

$$H_2O + e^- \rightarrow H_2O^v + e^- \quad \text{(R3)}$$

$$H_2O^v \rightarrow H^* + OH^* \quad \text{(R4)}$$

$$CH_4 + e^- \rightarrow CH_4^v + e^- \quad \text{(R5)}$$

$$CH_4^v \rightarrow CH_3^* + H^* \quad \text{(R6)}$$

$$CO_2 + e^- \rightarrow CO + O + e^- \quad \text{(R7)}$$

$$CO_2 + e^- \rightarrow CO_2^v + e^- \quad \text{(R8)}$$

$$CO_2^v + 2H \rightarrow CO + H_2O \quad \text{(R9)}$$

$$CO_2^v + O^{2-}* \rightarrow CO_3^{2-}* \quad \text{(R10)}$$

$$CH_3^* + CO_3^{2-}* \rightarrow CH_3COO^* + O^{2-}* \quad \text{(R11)}$$

$$CO_2^v + CH_3^* \rightarrow CH_3COO^* \quad \text{(R12)}$$

$$CH_3COO^* + 2H^* \rightarrow CH_3CHO^* + OH^* \quad \text{(R13)}$$

## 4. Conclusion

This study examined the plasma–catalyst hybrid process and revealed the products formed on the surface, as well as the corresponding reaction pathways of Cu nanoparticles on ZnO catalysts irradiated by DBD-activated Ar/ $CO_2$/$CH_4$/$H_2$ via *in situ* RS and DFT calculations. $CH_3COO$ was produced as the reaction product of DBD-activated gas on a Cu/ZnO catalyst. After the reaction, $CH_3CHO$ was produced by irradiation with DBD-activated $H_2O$. As a characteristic reaction, $CH_3COO$ was generated by the vibrationally excited $CO_2$ and $CH_4$ by DBD. Similarly, $CH_3CHO$ was generated by vibrationally excited $H_2O$ with $CH_3COO$. This study also revealed the effects of activated $H_2$ and $H_2O$, which are by-products of $CO_2$ and $CH_4$. These are known from the *in situ* measurements during plasma irradiation. Future investigation of the reaction pathway is required through *in situ* evaluation by Fourier transform infrared spectroscopy can complement the results obtained from RS.

## Acknowledgements

This project was supported by the JST CREST (JPMJCR19R3). Z. S. acknowledge the financial support from the China Scholarships Council program (201707040056).

## References

[1] Quadrelli E. A., Centi G., Duplan J-L., and Perathoner S., Carbon dioxide recycling: Emerging large-scale technologies with industrial potential, *ChemSusChem*, Vol. 4 (9), pp. 1194–1215, 2011.

[2] He M., Sun Y., and Han B., Green carbon science: Scientific basis for integrating carbon resource processing, utilization, and recycling, *Angew. Chem. Int. Ed*., Vol. 52 (37), pp. 9620–9633, 2013.

[3] Grim R. G., To A. T., Farberow C. A., Hensley J. E., Ruddy D. A., and Schaidle J. A., Growing the bioeconomy through catalysis: A review of recent advancements in the production of fuels and chemicals from syngas-derived oxygenates, *ACS Catal*., Vol. 9 (5), pp. 4145–4172, 2019.

[4] Hanaoka T., Hiasa S., and Edashige Y., Syngas production by gasification of aquatic biomass with $CO_2$/$O_2$ and simultaneous removal of $H_2S$ and COS using char obtained in the gasification, *Biomass Bioenergy*, Vol. 59, pp. 448–457, 2013.

[5] Centi G., and Perathoner S., Opportunities and prospects in the chemical recycling of carbon dioxide to fuels, *Catal*.

*Today*, Vol. 148 (3–4), pp. 191–205, 2009.
[6] Le M., Ren M., Zhang Z., Sprunger P. T., Kurtz R. L., and Flake J. C., Electrochemical reduction of $CO_2$ to $CH_3OH$ at copper oxide surfaces, *J. Electrochem. Soc*., Vol. 158 (5), pp. E45–E49, 2011.
[7] Wang W-H., Himeda Y., Muckerman J. T., Manbeck G. F., and Fujita E., $CO_2$ hydrogenation to formate and methanol as an alternative to photo- and electrochemical $CO_2$ reduction, *Chem. Rev*., Vol. 115 (23), pp. 12936–12973, 2015.
[8] Bogaerts A., Tu X., Whitehead J. C., Centi G., Lefferts L., Guaitella O., Azzolina-Jury F., Kim H. H., Murphy A. B., Schneider W. F., Nozaki T., Hicks J. C., Rousseau A., Thevenet F., Khacef A., and Carreon M., The 2020 plasma catalysis roadmap, *J. Phys. D. Appl. Phys*., Vol. 53 (44), pp. 443001, 2020.
[9] Kim H-H., Abdelaziz A. A., Teramoto Y., Nozaki T., Hensel K., Mok Y-S., Saud S., Nguyen B. D., Lee H. D., and Kang S. W., Interim report of plasma synthesis: Footprints in the past and blueprints for the future, *Int. J. Plasma Environ. Sci. Technol*., Vol. 15 (1), pp. e01004, 2021.
[10] Mehta P., Barboun P., Go D. B., Hicks J. C., and Schneider W. F., Catalysis enabled by plasma activation of strong chemical bonds: A review, *ACS Energy Lett*., Vol. 4 (5), pp. 1115–1133, 2019.
[11] Sheng Z., Watanabe Y., Kim H-H., Yao S., and Nozaki T., Plasma-enabled mode-selective activation of $CH_4$ for dry reforming: First touch on the kinetic analysis, *Chem. Eng. J*., Vol. 399, pp. 125751, 2020.
[12] Adrianto D., Sheng Z., and Nozaki T., Mechanistic study on nonthermal plasma conversion of $CO_2$, *Int. J. Plasma Environ. Sci. Technol*., Vol. 14 (1), pp. e01003, 2020.
[13] Mei D., Zhu X., Wu C., Ashford B., Williams P. T., and Tu X., Plasma-photocatalytic conversion of $CO_2$ at low temperatures: Understanding the synergistic effect of plasma-catalysis, *Appl. Catal. B Environ*., Vol. 182, pp. 525–532, 2016.
[14] Kano M., Satoh G., and Iizuka S., Reforming of carbon dioxide to methane and methanol by electric impulse low-pressure discharge with hydrogen, *Plasma Chem. Plasma Process*., Vol. 32, pp. 177–185, 2012.
[15] Wang L., Yi Y., Guo H., and Tu X., Atmospheric pressure and room temperature synthesis of methanol through plasma-catalytic hydrogenation of $CO_2$, *ACS Catal*., Vol. 8 (1), pp. 90–100, 2018.
[16] Liu L., Das S., Chen T., Dewangan N., Ashok J., Xi S., Borgna A., Li Z., and Kawi S., Low temperature catalytic reverse water-gas shift reaction over perovskite catalysts in DBD plasma, *Appl. Catal. B Environ*., Vol. 265, pp. 118573, 2020.
[17] Li J., Ma C., Zhu S., Yu F., Dai B., and Yang D., A Review of recent advances of dielectric barrier discharge plasma in catalysis, *Nanomaterials*, Vol. 9, pp. 1428, 2019.
[18] Nozaki T., Miyazaki Y., Unno Y., and Okazaki K., Energy distribution and heat transfer mechanisms in atmospheric pressure non-equilibrium plasmas, *J. Phys. D. Appl. Phys*., Vol. 34 (23), pp. 3383–3390, 2001.
[19] Lu H., Yao X., Li J., Yao S., Wu Z., Zhang H., Lin H., and Nozaki T., Mechanism on the plasma-catalytic oxidation of graphitic carbon over Au/γ-$Al_2O_3$ by in situ plasma DRIFTS-mass spectrometer, *J. Hazard. Mater*., Vol. 396, pp. 122730, 2020.
[20] Mino L., Spoto G., and Ferrari A. M., $CO_2$ capture by $TiO_2$ anatase surfaces: A combined DFT and FTIR study, *J. Phys. Chem. C*, Vol. 118 (43), pp. 25016–25026, 2014.
[21] Kuhl K. P., Cave E. R., Abram D. N., and Jaramillo T. F., New insights into the electrochemical reduction of carbon dioxide on metallic copper surfaces, *Energy Environ. Sci*., Vol. 5, pp. 7050–7059, 2012.
[22] Vuurman M. A., and Wachs I. E., In situ Raman spectroscopy of alumina-supported metal oxide catalysts, *J. Phys. Chem*. Vol. 96 (12), pp. 5008–5016, 1992.
[23] Meyer B., and Marx D., Density-functional study of Cu atoms, monolayers, films, and coadsorbates on polar ZnO surfaces, *Phys. Rev. B*, Vol. 69, pp. 235420, 2004.
[24] Raza W., Faisal S. M., Owais M., Bahnemann D., and Muneer M., Facile fabrication of highly efficient modified ZnO photocatalyst with enhanced photocatalytic, antibacterial and anticancer activity, *RSC Adv*., Vol. 6, 78335–78350, 2016.
[25] Stephens P. J., Devlin F. J., Chabalowski C. F., and Frisch M. J., Ab initio calculation of vibrational absorption and circular dichroism spectra using density functional force fields, *J. Phys. Chem*., Vol. 98 (45), pp. 11623–11627, 1994.
[26] https://www.basissetexchange.org/
[27] Frisch M. J., Trucks G. W., Schlegel H. B., Scuseria G. E., Robb M. A., Cheeseman J. R., Scalmani, G., Barone V., Petersson G. A., Nakatsuji H., Li X., Caricato M., Marenich A. V., Bloino J., Janesko B. G., Gomperts R., Mennucci B., Hratchian H. P., Ortiz J. V., Izmaylov A. F., Sonnenberg J. L., Williams-Young D., Ding, F., Lipparini, F., Egidi F., Goings J., Peng B., Petrone A., Henderson T., Ranasinghe D., Zakrzewski V. G., Gao J., Rega N., Zheng G., Liang W., Hada M., Ehara M., Toyota K., Fukuda R., Hasegawa J., Ishida M., Nakajima T., Honda Y., Kitao O., Nakai H., Vreven T., Throssell K., Montgomery J. A. Jr., Peralta J. E., Ogliaro F., Bearpark M. J., Heyd J. J., Brothers E. N., Kudin K. N., Staroverov V. N., Keith T. A., Kobayashi R., Normand J., Raghavachari K., Rendell A. P., Burant J. C., Iyengar S. S., Tomasi J., Cossi M., Millam J. M., Klene M., Adamo C., Cammi R., Ochterski J. W., Martin R. L., Morokuma K., Farkas O., Foresman J. B., and Fox, D. J., Gaussian 16, Revision C.01, Gaussian, Inc., Wallingford CT, 2016.

[28] Azpiroz J. M., and De Angelis F., DFT/TDDFT study of the adsorption of N3 and N719 dyes on ZnO(10$\bar{1}$0) surfaces, *J. Phys. Chem. A*, Vol. 118 (31), pp. 5885–5893, 2014.
[29] Fink K., Ab initio cluster calculations on the electronic structure of oxygen vacancies at the polar ZnO (000$\bar{1}$) surface and on the adsorption of $H_2$, CO, and $CO_2$ at these sites, *Phys. Chem. Chem. Phys*., Vol. 8, pp. 1482–1489, 2006.
[30] Staemmler V., Fink K., Meyer B., Marx D., Kunat M., Gil Girol S., Burghaus U., and Wöll C., Stabilization of polar ZnO surfaces: Validating microscopic models by using CO as a probe molecule, *Phys. Rev. Lett*., Vol. 90 (10), pp. 106102, 2003.
[31] Shi B., Su Y., Duan Y., Chen S., and Zuo W., A nanocomposite prepared from copper(II) and nitrogen-doped graphene quantum dots with peroxidase mimicking properties for chemiluminescent determination of uric acid, *Mikrochim. Acta*., Vol 186, pp. 397, 2019.
[32] Collado L., Reynal A., Fresno F., Barawi M., Escudero C., Perez-Dieste V., Coronado J. M., Serrano P., Durrant J., and de la Peña O'Shea V. A., Unravelling the effect of charge dynamics at the plasmonic metal/semiconductor interface for $CO_2$ photoreduction, *Nat. Commun*., Vol 9, pp. 4936, 2018.
[33] Ye H., Na W., Gao W., and Wang H., Carbon-modified CuO/ZnO catalyst with high oxygen vacancy for $CO_2$ hydrogenation to methanol, *Energy Technol*., Vol. 8, pp. 1–13, 2020.
[34] Sharifi M., Haghighi M., Rahmani F., and Karimipour S., Syngas production via dry reforming of $CH_4$ over Co- and Cu-promoted Ni/$Al_2O_3$-$ZrO_2$ nanocatalysts synthesized via sequential impregnation and sol-gel methods, *J. Nat. Gas Sci. Eng*., Vol. 21, pp. 993–1004, 2014.
[35] Sheng Z., Kim H-H., Yao S., and Nozaki T., Plasma-chemical promotion of catalysis for $CH_4$ dry reforming: unveiling plasma-enabled reaction mechanisms, *Phys. Chem. Chem. Phys*., Vol. 22, pp. 19349–19358, 2020.
[36] Rhaiem A. B., Hlel F., Guidara K., and Gargouri M., Vibrational study of $[(CH_3)_4N]_2Cu_{0.5}Zn_{0.5}Cl_4$, *Spectrochim. Acta. A*., Vol. 66, pp. 1107–1109, 2007.
[37] Shido T., and Iwasawa Y., Reactant-promoted reaction mechanism for water-gas shift reaction on ZnO, as the genesis of surface catalysis., *J. Catal.*, Vol. 129 (2), pp. 343–355, 1991.
[38] Petersen P., and Krasser W., Surface enhanced Raman scattering from a ternary catalyst Cu/ZnO/$Al_2O_3$ under reaction conditions, *Appl. Surf. Sci*., Vol. 103 (1), pp. 91–100, 1996.
[39] Gao L. Z., and Au C. T., $CO_2$ hydrogenation to methanol on a $YBa_2Cu_3O_7$ catalyst, *J. Catal*., Vol. 189 (1), pp. 1–15, 2000.
[40] Hundt P. M., Jiang B., van Reijzen M. E., Guo H., and Beck R. D., Vibrationally promoted dissociation of water on Ni(111), *Science*., Vol 344, pp. 504–507, 2014.
[41] Riguang Z., Hongyan L., Lixia L., Zhong L., and Baojun W., A DFT study on the formation of $CH_3O$ on $Cu_2O$ (111) surface by $CH_3OH$ decomposition in the absence or presence of oxygen, *Appl. Surf. Sci*., Vol. 257 (9), pp. 4232–4238, 2011.
[42] Brodsky M. H., Cardona M, and Cuomo J. J., Infrared and Raman spectra of the silicon-hydrogen bonds in amorphous silicon prepared by glow discharge and sputtering, *Phys. Rev. B.*, Vol. 16, pp. 3556–3571, 1977
[43] Pietanza L. D., Colonna G., D'Ammando G., Laricchiuta A., and Capitelli M., Electron energy distribution functions and fractional power transfer in "cold" and excited $CO_2$ discharge and post discharge conditions, *Phys. Plasmas*, Vol. 23 (1), pp. 013515, 2016.
[44] Yang R., Zhang Y., and Tsubaki N. Rideal-type reaction of formate species with alcohol: A key step in new low-temperature methanol synthesis method, *Catal. Commun*., Vol. 8 (11), pp. 1829–1833, 2007.
[45] Quan J., Muttaqien F., Kondo T., Kozarashi T., Mogi T., Imabayashi T., Hamamoto Y., Inagaki K., Hamada I., Morikawa Y., and Nakamura J., Vibration-driven reaction of $CO_2$ on Cu surfaces via Eley–Rideal-type mechanism, *Nat. Chem*., Vol. 11, pp. 722–729, 2019.
[46] Quan J., Kondo T., Wang G., and Nakamura J., Energy transfer dynamics of formate decomposition on Cu(110), *Angew. Chem. Int. Ed*., Vol. 56 (13), pp. 3496–3500, 2017.